Supporting Information

Carrier dynamics tailored by electron/hole trapping domains in asymmetric graphitic carbon nitride for superior photocatalytic hydrogen evolution

Hao Yang[a], Shaodong Sun[a,b], Honghong Wang[a], Qing Yang[a,b], Anran Chen[c]*, and Jie Cui[a,b]**

[a]Engineering Research Center of Conducting Materials and Composite Technology, Ministry of Education; Shaanxi Engineering Research Center of Metal-Based Heterogeneous Materials and Advanced Manufacturing Technology; Shaanxi Province Key Laboratory for Electrical Materials and Infiltration Technology; School of Materials Science and Engineering, Xi'an University of Technology, Xi'an 710048, Shaanxi, People's Republic of China.

[b]Shaanxi Laboratory of Advanced Materials, Xi'an 710021, Shaanxi, People's Republic of China.

[c]Yunnan Key Laboratory of Electromagnetic Materials and Devices, School of Materials and Energy, Yunnan University, Kunming 650091, Yunnan, People's Republic of China.

E-mail: sdsun@xaut.edu.cn (S. D. Sun), anran@ynu.edu.cn (A. R. Chen), cuijie@xaut.edu.cn (J. Cui).

Table of Contents

S3. Supplementary Tables

S1. Experimental section

S1.1 Materials and chemical reagents

Melamine (MA), cyanuric acid, triethanolamine (TEOA) and 2,2,6,6-tetramethylpiperidine-1-oxyl (TEMPO) were purchased from Shanghai Aladdin Biochemical Technology Co., Ltd. Barbituric acid (BA), chloroplatinic acid (H_2PtCl_6) were purchased from Shanghai Macklin Biochemical Co., Ltd. The anhydrous ethanol was purchased from Tianjin Fuyu Fine Chemical Co., Ltd. Sodium sulfate (Na_2SO_4) was purchased from Shanghai Yi'en chemical technology Co., Ltd. All the reagents were used without further purification. Ultrapure water was used throughout the experiment.

S1.2 Characterization

The morphologies of the samples were obtained by scanning electron microscope (SEM, JSM-7000F), and transmission electron microscope (TEM, JEM-2100). Powder X-ray diffraction (XRD) analyses were collected on a Bruker D8 Advanced X-ray diffractometer using Cu Kα radiation (40 KV, 40 mA). Fourier transform infrared (FTIR) spectra for all samples were conducted by Bruker Tensor 27 spectrometer scanning. X-ray photoelectron spectroscopy (XPS) and their valence-band spectra were recorded by a Thermofisher scalable 250xi instrument equipped with an Al Kα X-ray source. The elemental determinations were measured by the element analyzer (UNICUBE - Elementar). The ^{13}C solid-state cross polarization magic angle spinning nuclear magnetic resonance (CP-MAS NMR) spectra were taken on a Bruker avance III 400 MHz. The Brunauer-Emmett-Teller (BET) surface areas of samples were recorded by the nitrogen adsorption-desorption method at 77 K on a Quantachrome apparatus. The pore size distribution curves were surveyed using the Barrett-Joyner-Halenda (BJH) model. The photoluminescence (PL, FluoroMax-4P) spectra were measured by a fluorescence spectrophotometer with an excitation wavelength of 350 nm. Temperature-dependent PL spectra (FLS1000) were measured by at 80 K, 100 K, 120 K, 140 K, 160 K, 180 K, 200 K, 220 K, 260 K and 300 K. The femtosecond transient absorption spectroscopy (fs-TA) was measured on a Helios pump-probe system from Ultrafast Systems LLC coupled with an amplified femtosecond laser system from Coherent. The optical parametric amplifier (TOPAS-800-fs) delivered a 350 nm pump pulse (~0.1 mW), which was generated by a Ti-sapphire regenerative amplifier (800 nm, 35 fs, 6 mJ/pulse, and 1 kHz repetition rate). The surface potentials were measured by in-situ KPFM on a Bruker Dimension Icon. The samples were dispersed in ethanol via sonication, then spin-coated onto ITO for

testing. Subsequently, the contact potential differences of the samples were recorded under dark and light irradiation, respectively. Contact angle measurements were taken on a KRUSS DSA100 contact angle meter. UV-visible diffuse reflectance spectra (UV-vis DRS, LAMBDA950) were recorded using a UV/vis/NIR spectrophotometer. Electron paramagnetic resonance (EPR) analyses were detected on an EMX nano BRUKER spectrometer.

S1.3 Photoelectrochemical test

The photoelectrochemical properties, including Mott-Schottky plots (M-S), electrochemical impedance spectra (EIS), and transient photocurrent response (TPR), and open circuit potential-time plots (OCPT), cyclic voltammetry curves (CV), linear sweep voltammetry curves (LSV) were evaluated in a 0.25 M Na_2SO_4 aqueous solution using an electrochemical workstation (CHI660E) with a three-electrode system under simulated visible light irradiation. The photocatalyst-coated F-doped tin oxide conductive glass (FTO), a Pt mesh, and an Ag/AgCl electrode acted as the working electrode, the counter electrode, and the reference electrode, respectively. The working electrode was prepared as follows: 10 mg of the photocatalyst was dispersed in 1 mL of Nafion solution (5 wt%) with the assistance of ultrasound. Then, the slurry was dropped onto a FTO with an exposed area of 1 cm × 1 cm and dried in the air to form a working electrode.

S1.4 Photocatalytic hydrogen evolution experiment

Photocatalytic hydrogen evolution reactions of samples were carried out by an online photocatalytic hydrogen generation system (Beijing Perfect-light Science & Technology Co., Ltd., China) with a 250 mL closed quartz reactor and a circulating water system. The light source was a 300 W Xe lamp (λ > 420 nm, Beijing Perfect-light, PLS-SXE300). The experiment process was described as follows: 50 mg of as-prepared samples were dispersed in 100 mL of the aqueous solution containing TEOA (10 vol%) as an electron donor, with ultrasound for 20 min. The H_2PtCl_6 aqueous solution acted as the source of the cocatalyst (3 wt% Pt) and was added to the suspension and irradiated for 60 min to ensure that the Pt was loaded tightly on the photocatalyst surface. Afterward, the reaction vessel was completely degassed to remove air before being further irradiated. The temperature of the reaction solution was maintained at 6℃ by cooling the circulating water system during the photocatalytic hydrogen evolution reaction.

The apparent quantum efficiency (AQE) for hydrogen evolution was measured using the same experimental conditions, except that the Xe lamp equipped with a band-pass filter (λ =

420 ± 10 nm, 450 ± 10 nm, 475 ± 10 nm, 550 ± 10 nm). The light intensity is obtained with an optical power meter (CEL-NP2000, Beijing). The AQE was calculated as follows:

$$P = \times A_R \quad \text{(Equation S1)}$$

$$N_P^i = \frac{Pt\lambda}{hc} \quad \text{(Equation S2)}$$

$$Ne = 2 \times {}^{n_{H_2}} \times N_A \quad \text{(Equation S3)}$$

$$AQE = \frac{N_e}{N_P^i} \times 100\% \quad \text{(Equation S4)}$$

S1.5 Computation methods

Differential charge density analysis and density of states of BCN and EHTD-CN were performed based on the density function theory (DFT) calculations implemented in the Vienna *ab* initio simulation package (VASP) code[1-4]. The projected augmented wave (PAW) method within the generalized gradient approximation of Perdew, Burke, and Ernzerhof (PBE) was selected to treat exchange-correlation effects[5]. To minimize the interaction between neighboring slabs, a 15 Å vacuum region was chosen as the periodic boundary condition. The energy cutoff was 500 eV. The atomic positions were relaxed until forces on each atom were less than 0.02 eV/Å. For the geometry optimization, a Monkhorst-Pack grid of 3×3×1 *k*-point was adopted. For the static calculations, a Monkhorst-Pack grid of 7×7×1 *k*-point was adopted. Then, based on the optimized crystal structure, the electronic structures were calculated.

The calculations of surface electrostatic potential, Frontier molecular orbital calculation, and Gibbs free energy for hydrogen absorption were carried out with the Gaussian software program with B3LYP and a 6-31G* basis set. The HOMO, LUMO distributions, and electrostatic potential (ESP) were obtained and mapped using the Multiwfn program and VMD software. The adsorption energy of H (ΔE_{H^*}) on BCN and EHTD-CN were defined as $E_{H^*} = E_{EHTD\text{-}CN+H^*} - E_{EHTD\text{-}CN} - 1/2E_{H2}$, where $E_{EHTD\text{-}CN+H^*}$ and $E_{EHTD\text{-}CN}$ are the total energies of $_{EHTD\text{-}CN}$ with and without H adsorption, respectively, and E_{H2} represents the energy of a H_2 molecule. The H adsorption free energy (ΔG_{H^*}) was defined as follows [6]:

$$G_{H^*} = E_{H^*} - \Delta E_{ZPE} - T\Delta S$$

where ΔE_{ZPE} and ΔS are the changes in zero-point energy and entropy between H desorption and adsorption, respectively.

S1.6 Probe-labeled EPR measurement

TEMPO-labeled EPR measurement for e^-: 1 mg of prepared samples (BCN, NTD-CN and EHTD-CN) were dispersed into 1 mL of deionized water (containing 10 vol% TEOA) and sonicated for 30 min. The 5 μL of TEMPO solution (10 mM) serving as a trapping agent for e^- was added into 45 μL of the above aqueous solution.

DMPO-labeled EPR measurement for $\bullet O_2^-$: 1 mg of prepared samples (BCN, NTD-CN and EHTD-CN) were dispersed into 1 mL of methanol and sonicated for 30 min. The 5 μL of DMPO serving as a trapping agent for $\bullet O_2^-$ was added into 45 μL of the above methanol solution.

Subsequently, the well-mixed solution was irradiated for 10 min with a 300 W xenon lamp as a light source. Next, the solution before and after illumination was drawn separately with a capillary tube and carefully placed into the sample chamber of the EPR spectrometer to obtain the EPR spectra. The scan number was set as 5 times.

S1.7 The calculation method for the built-in electric field

The strength of the built-in electric field can be described by Poisson's equation[7-9]:

$$E = \frac{eN_d}{\varepsilon_0 \varepsilon_r} W(V_s) \quad \text{(Equation S5)}$$

where eN_d is the surface charge density, here defined as $-\rho$; The ε_0 and ε_r are the dielectric constant of the graphitic carbon nitride and vacuum dielectric constant, respectively. W(Vs) is the width of the space charge region, which can be described as:

$$W(V_s) = \sqrt{\frac{2\varepsilon_0 \varepsilon_r V_s}{eN_d}} \quad \text{(Equation S6)}$$

Therefore,

$$E = \sqrt{\frac{-2\rho V_s}{\varepsilon_0 \varepsilon_r}} \quad \text{(Equation S7)}$$

Here, V_S is the surface response voltage, which can be measured by OCPT. As illustrated in Figure S1, given that the Fermi level of the n-type semiconductor locates above its surface states, when the photocatalyst is subjected to light exposure, electrons near the surface travel across the interface to the catalyst surface. This induces significant band bending and, consequently, a photovoltage signal that qualifies as a surface response voltage. When the light is extinguished, the robust built-in electric field effectively curbs charge recombination, thereby resulting in a slow decay (Figure 7i).

In addition, ρ can be measured by integrating the step region of the photocurrent response curve.

Normalizing the strength of the built-in electric field for BCN is to 1, the relative built-in electric field strength is:

$$= \sqrt{\frac{\rho\ Vs}{(\rho\ Vs)_{BCN}}} \quad \text{(Equation S8)}$$

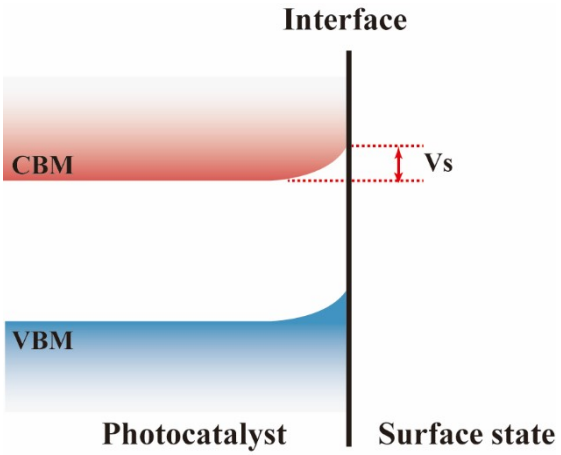

Figure S1. Space-charge region of an n-type semiconductor at the interface.

S1.8 The calculation method for other data

a) Calculations for charge carrier density (N_D)

According to the Equation S5 and Equation S6, the charge carrier density (N_D) of various photocatalytic materials can be calculated:

$$\frac{1}{C^2} = \left[\frac{2}{e\varepsilon\varepsilon_0}\right] \times \left(E - E_{fb} - \frac{k_B T}{E}\right) \quad \text{(Equation S9)}$$

$$N_D = \left(\frac{2}{e\varepsilon\varepsilon_0}\right) \times \left(\frac{d\frac{1}{C^2}}{dE}\right)^{-1} \quad \text{(Equation S10)}$$

where C refers to the capacitance of space charge layer, e represents the elementary charge (1.602×10^{-19} C), ε and ε_0 are the dielectric constant of graphitic carbon nitride (ε = 5.25) and vacuum permittivity ($\varepsilon_0 = 8.85 \times 10^{-14}$ F/m^2), respectively, E and E_{fb} denote the applied bias potential and flat-band potential, k_B and T signify the Boltzmann constant (1.38×10^{-23} J/K) and Kelvin temperature, respectively [8].

b) Calculations for exciton binding energy (E_b):

$$I(T) = \frac{I_0}{1 + A \times \exp(\frac{-E_b}{k_B T})} \quad \text{(Equation S11)}$$

where I_0 and I(T) represent the PL intensity at 0 K and tested temperature (T), k_B and stand for the Boltzmann constant (1.38×10^{-23} J/K) and Kelvin temperature, respectively [10].

Calculations for excitons dissociation efficiency (DE):

$$DE = \exp(\frac{-E_b}{k_B T}) \quad \text{(Equation S12)}$$

where $k_B T \approx 25$ meV at room temperature.

S2. Supplementary Figures and Tables

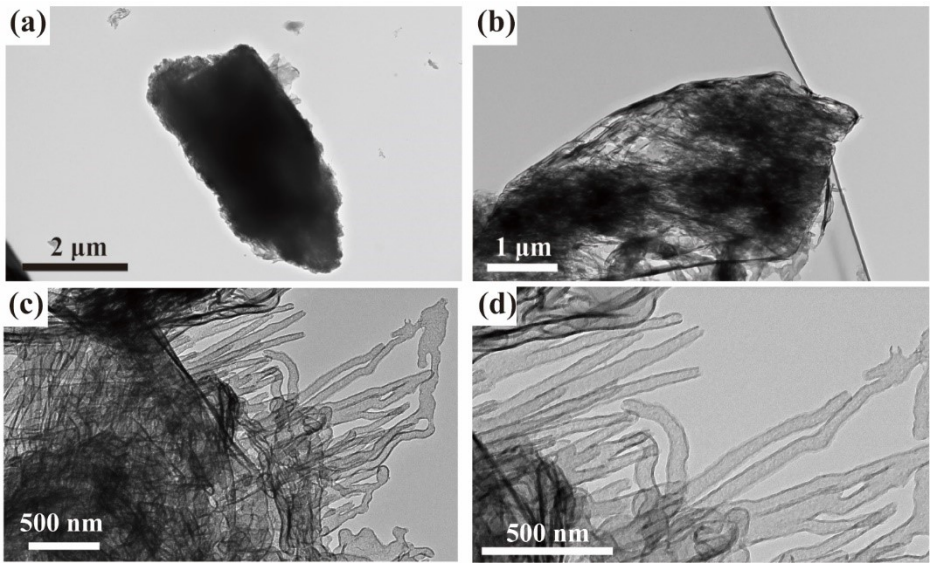

Figure S2. TEM images of (a) BCN, (b) NTD-CN, and (c–d) EHTD-CN.

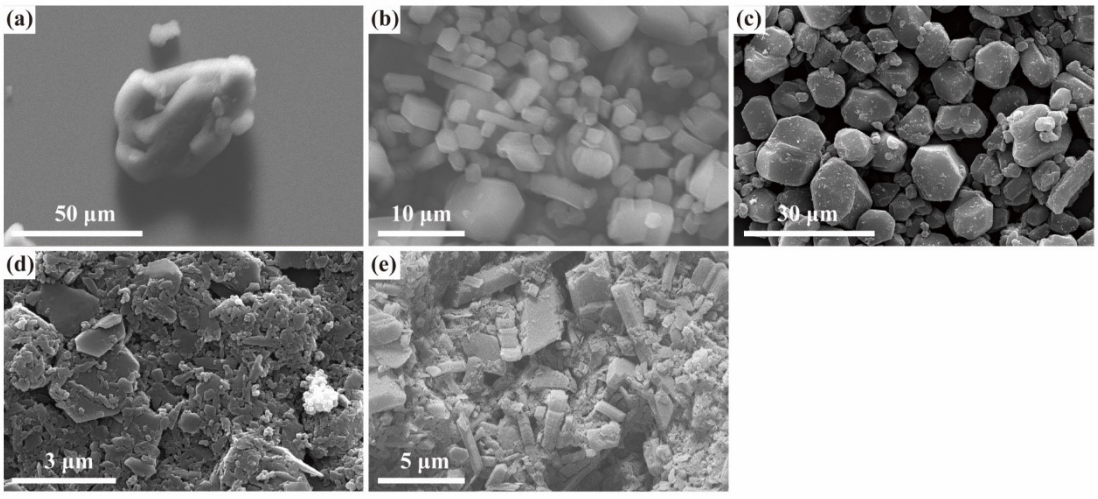

Figure S3. SEM images of (a) commercial melamine and (b) MCA-NTD, (c) MCA-HTD, (d) MCA-ETD, (e) MCA-EHTD supramolecular precursors.

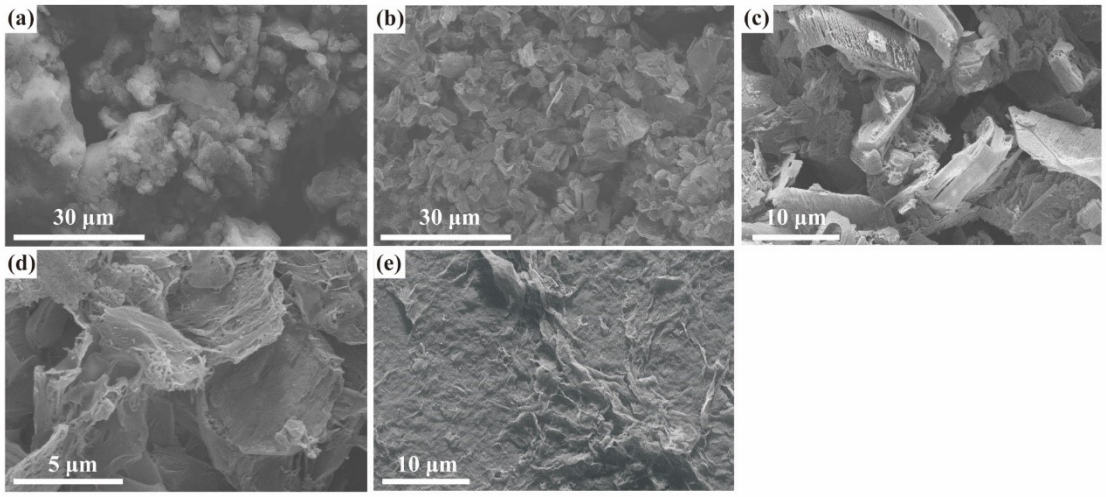

224

225 **Figure S4.** SEM images of (a) BCN, (b) NTD-CN, (c) HTD-CN, (d) ETD-CN, (e) EHTD-CN samples.

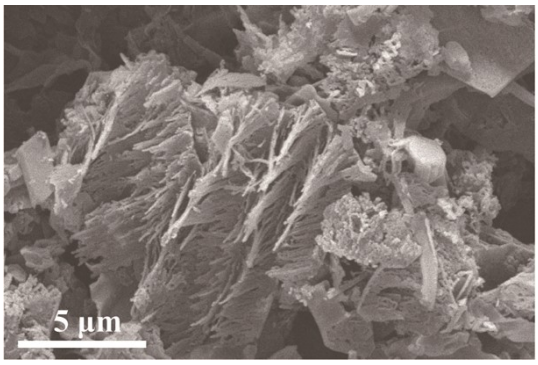

226

227 **Figure S5.** SEM image of EHTD-CN-BA-0.6.

228 SEM images of commercial melamine and various precursors are presented in Figure
229 S3. As expected, commercial melamine exhibits an irregular blocky morphology.
230 Owing to the similar molecular structure of barbituric acid to melamine and cyanuric
231 acid, coupled with its low addition amount, the morphologies of MCA-NTD and MCA-
232 HTD supramolecular intermediates show no significant distinction, both displaying a
233 characteristic hexagonal prism appearance. Since the solvent polarity affects the
234 hydrogen bonding strength between supramolecular building blocks, weakly polar
235 ethanol impedes the self-assembly process [11], leading to a morphological
236 transformation in MCA-ETD from prismatic structures to worm-like agglomerates.
237 Subsequently, the morphology of MCA-EHTD undergoes further fragmentation upon
238 the coexistence of barbituric acid and ethanol. These observations are in good

agreement with the morphological evolution of synthesized g-C_3N_4 samples (Figure S4–Figure S7).

Consistent with the evolution principle observed in the supramolecular precursors, BCN exhibits significant bulk agglomeration. In contrast, NTD-CN and HTD-CN, derived from the polymerization of hexagonal prism-like MCA-NTD and MCA-HTD supramolecular intermediates, largely inherit this morphology. This structural retention stems from the loosely π-π stacking of conjugated planes, forming loosely accordion-like microstructure. The modulation of supramolecular self-assembly process by weakly polar ethanol solvent also affects the morphology of final products. As shown in Figure S4d, the original microstructure of NTD-CN collapses into lamellar stacked aggregates. The morphology of EHTD-CN undergoes further exfoliation, resulting in a sheet-like structure.

When the addition amount of barbituric acid is further increased, its similar molecular structure to melamine and cyanuric acid, combined with enhanced protonation effects, partially improves the supramolecular self-assembly process. Consequently, EHTD-CN-BA-0.6 displays a partially damaged accordion-like morphology, accompanied by irregular aggregates.

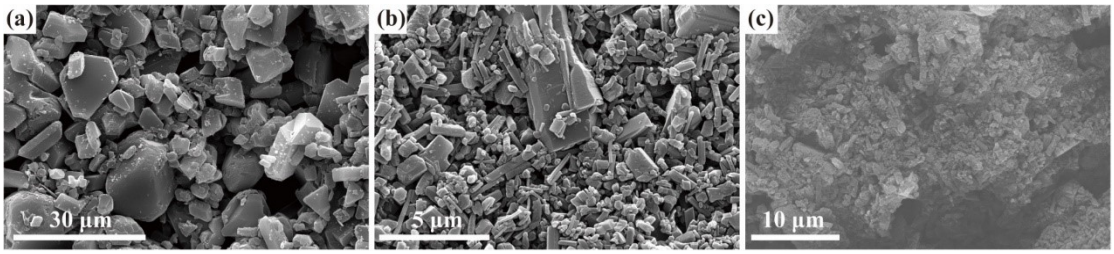

Figure S6. SEM images of (a) MCA-OH-1, (b) MCA-OH-3, and (c) MCA-OH-4.

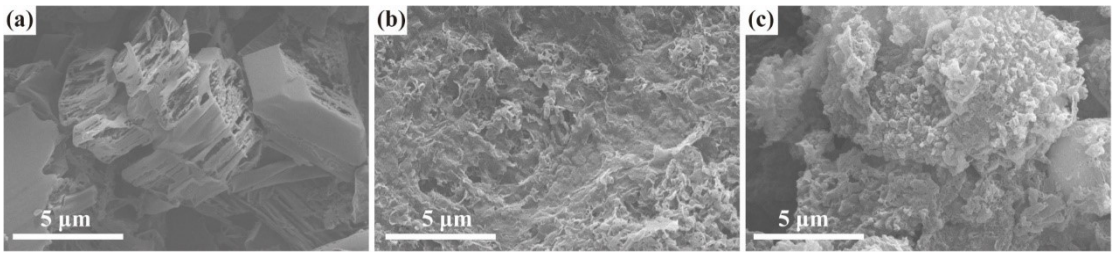

Figure S7. SEM images of (a) EHTD-CN-OH-1, (b) EHTD-CN-OH-3, and (c) EHTD-CN-OH-4.

The regulatory effect of ethanol on the morphology evolution of supramolecular intermediates and g-C_3N_4 samples was investigated under the fixed barbituric acid addition. Specifically, in the strongly polar aqueous solvent, robust hydrogen bonding drives the dense stacking of supramolecular planes into hexagonal prism morphologies. The addition of ethanol impedes hydrogen bond formation between the molecules of melamine, cyanuric acid, and barbituric acid. Consequently, the hexagonal prisms progressively fragment until the weakened hydrogen bonding can no longer sustain the 3D structure of supramolecular intermediates, collapsing into irregular nanoparticles. As shown in Figure S3 and Figure S6, as the proportion of ethanol in the mixed solvent increases, the micro-morphology of MCA supramolecules gradually transforms from hexagonal prisms (MCA-NTD and MCA-HTD) to irregular microparticles (MCA-OH-1), then gradually breaks into a mixture of fragmented micro-blocks and small particles (MCA-OH-3), and finally becomes nanoscale particles (MCA-OH-4). This trend aligns consistently with the morphological evolution observed in the g-C_3N_4 samples (Figure S4 and Figure S7). When deionized water used as the solvent, the EHTD-CN-OH-0 (HTD-CN) exhibits a characteristic accordion-like morphology. As the ethanol/water ratio increases, the morphology of EHTD-CN-OH series samples

transforms from fragmented accordion-like assemblies to exfoliated sheets. Subsequently, driven by a self-generated gas-bubble templating effect [12], spherical bubble-like structures gradually emerge on the surface of sheet-like assemblies. This ultimately transforms the morphology into a 3D architecture composed of stacked spherical bubble-like structures. Collectively, these structural evolutions demonstrate that barbituric acid and ethanol can synergistically modulate the morphology of EHTD-CN.

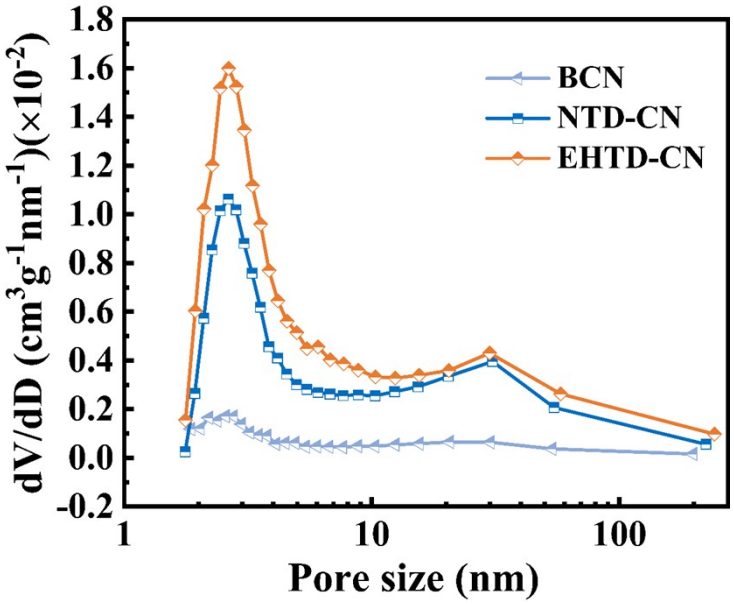

284

285 **Figure S8.** Pore size distribution curves of BCN, NTD-CN and EHTD-CN.

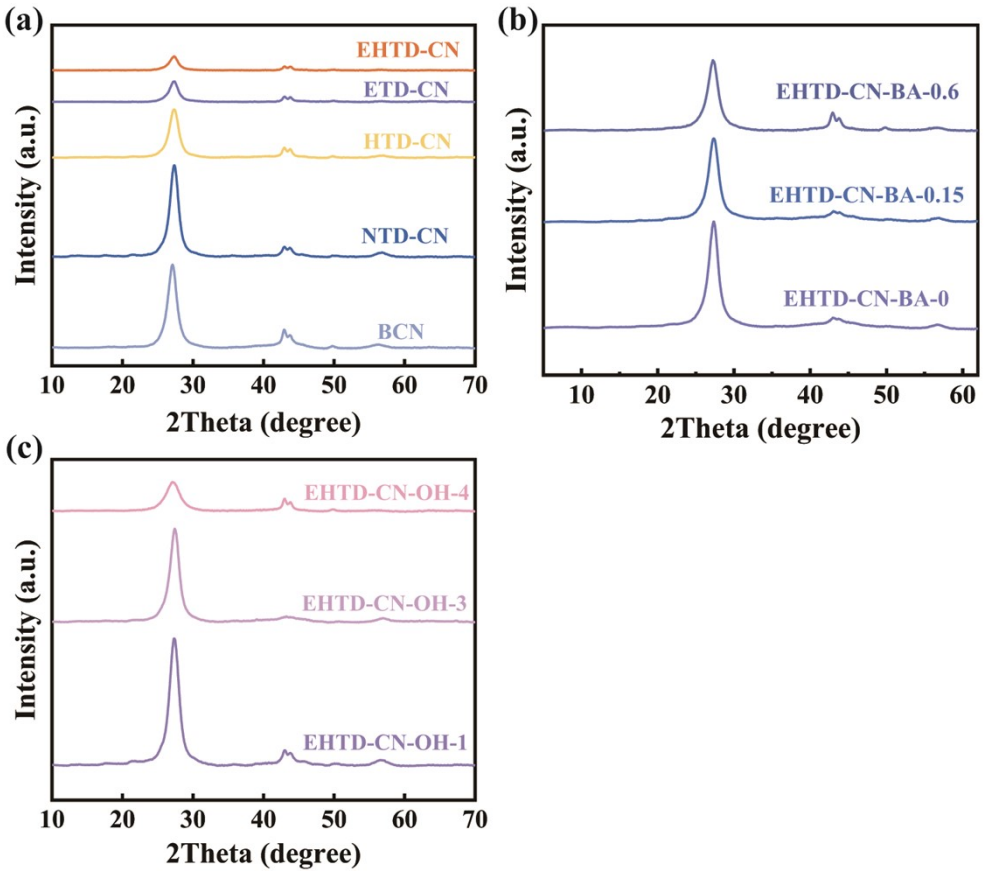

Figure S9. (a) XRD patterns of BCN, NTD-CN, HTD-CN, ETD-CN and EHTD-CN. (b) XRD patterns of EHTD-CN-BA0 (ETD-CN), EHTD-CN-BA0.1 and EHTD-CN-BA0.6. (c) XRD patterns of EHTD-CN-OH-1, EHTD-CN-OH-3 and EHTD-CN-OH-4.

The influences of the concentration of pyrimidine structures (Figure S9b) and hydroxyl groups (Figure S9c) on the physical structure of EHTD-CN were also investigated. The EHTD-CN-BA series samples exhibit distinct diffraction peaks near 27.3°. Consistent with the evolution trend observed in SEM images, the diffraction peak intensity shows no significant variation, owing to the similar molecular structure of barbituric acid to melamine and cyanuric acid, coupled with the enhanced acidic environment during supramolecular self-assembly. Conversely, the participation pf weakly polar ethanol disrupts the ordered self-assembly of molecular building blocks, resulting in a progressive attenuation of diffraction peak intensity in EHTD-CN-OH series samples. This also reflects the successful introduction of hydroxyl functional groups.

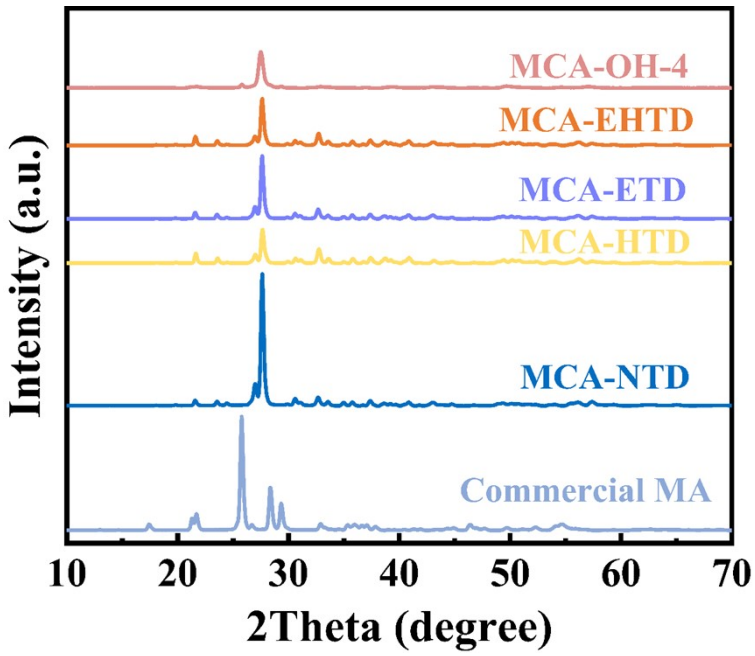

Figure S10. XRD patterns of commercial MA and MCA-EHTD series precursors.

As shown in Figure S10, the powder XRD pattern of commercial melamine corresponds to monoclinic phase structure. Subsequently, MCA-NTD undergoes a transformation to an orthorhombic phase with strong diffraction peaks. This indicates that melamine and cyanuric acid undergo supramolecular self-assembly via hydrogen bonding in polar aqueous solvent, resulting in their regular stacking into the hexagonal prism morphology (Figure S3b). The incorporation of ETD and HTD does not alter the fundamental molecular framework of supramolecular intermediate. However, it leads to a gradually decrease in diffraction intensity and concomitant fragmentation of the morphology (Figure S3e).

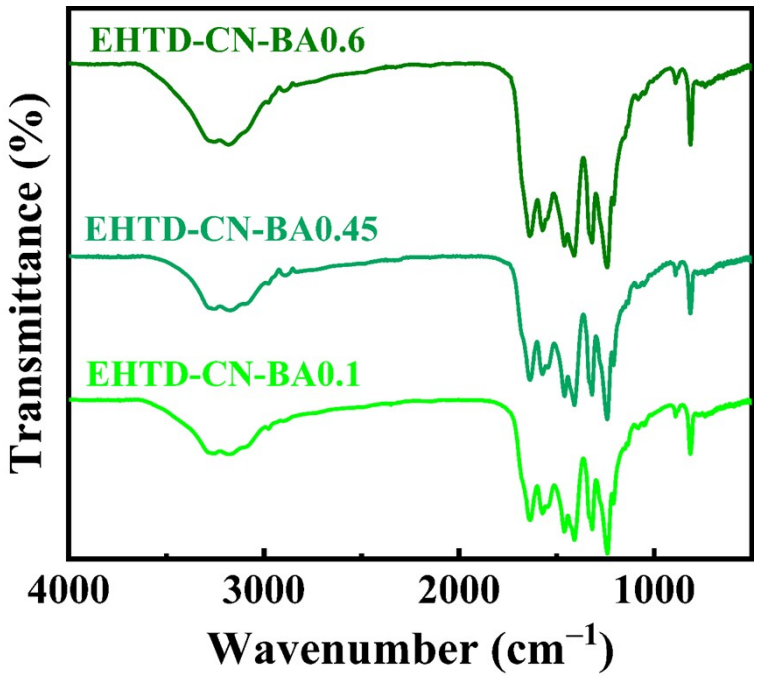

Figure S11. FTIR spectra of EHTD-CN-BA0.1, EHTD-CN-BA0.45 and EHTD-CN-BA0.6.

As shown in Figure S11, increasing barbituric acid addition during supramolecular self-assembly induces no significantly changes in the FTIR spectra of EHTD-CN-BA series samples, except for enhanced vibrational intensity of aromatic heterocycles. This confirms that pyrimidine ring incorporation does not disrupt the fundamental framework of g-C_3N_4.

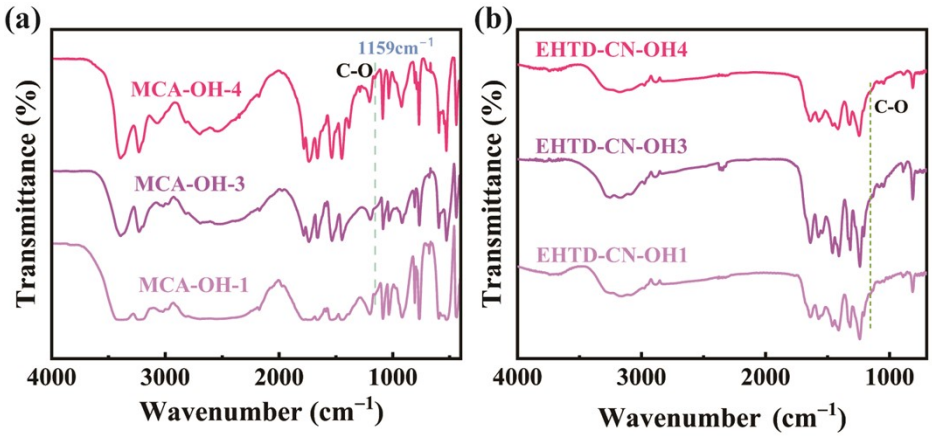

Figure S12. FTIR spectra of supramolecular intermediates and their derived EHTD-CN-OH-1, EHTD-CN-OH-3 and EHTD-CN-OH-4.

The effect of ethanol/water volume ratio on the molecular structures of supramolecular intermediates and corresponded g-C_3N_4 samples was further investigated (Figure S12). With increasing ethanol proportion, the intensity of C-O breathing vibration mode at 1159 cm^{-1} and asymmetric stretching vibration of adsorbed water/hydroxyl groups around 3280 cm^{-1} in MCA-OH series supramolecular intermediates gradually increases. These characteristic vibrations persist after polymerization of the supramolecular intermediates into EHTD-CN-OH series samples. This result demonstrates that the successful grafting of hydroxyl functional groups at the edges of heptazine framework.

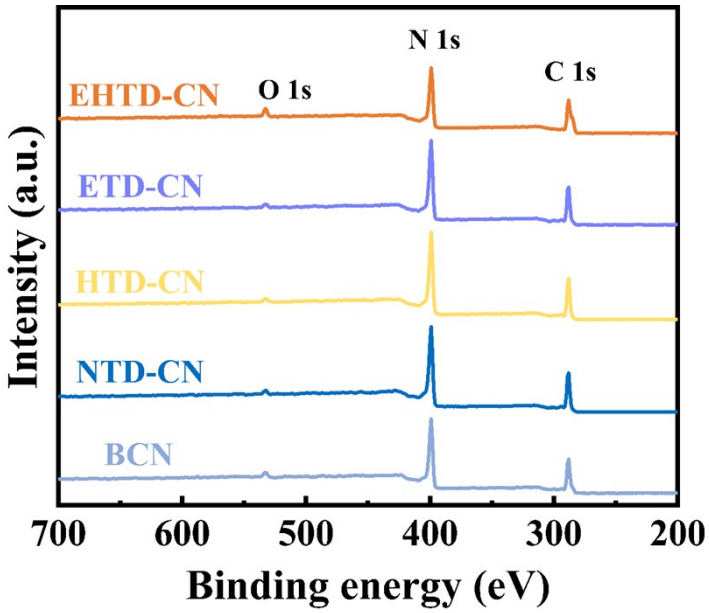

Figure S13. XPS spectra of full survey spectra of BCN, NTD-CN, HTD-CN, ETD-CN and EHTD-CN.

Table S1. The elemental analyses of samples determined by organic element analyzer.

Samples	Weight ratio (wt.%)				Atomic ratio (at.%)			
	N	C	H	O	N	C	H	C/N
BCN	60.956	34.677	2.127	11.913	46.56	30.87	22.56	0.663
NTD-CN	59.354	34.199	2.303	13.257	45.22	30.40	24.39	0.672
EHTD-CN	59.943	34.788	2.685	15.187	43.49	29.44	27.07	0.677

Elemental contents of N, C, H, and O in BCN, NTD-CN, and EHTD-CN were measured using an elemental analyzer. The N atom content in NTD-CN decreases significantly, owing to the hydrolysis of terminal amino groups during the supramolecular self-assembly. Meanwhile, its C/N ratio of 0.672 is closer to the theoretical value of 0.67 for melon-based g-C_3N_4, indicating that the supramolecular self-assembly is beneficial for reorganizing the molecular structure and avoiding the formation of structural defects. Subsequently, the increased C/N ratio of EHTD-CN confirms the incorporation of pyrimidine rings. Although measured O content exceeds actual values due to surface adsorbed H_2O and O_2 from ambient exposure, EHTD-CN demonstrates substantially higher O and H content than those in BCN and NTD-CN, confirming

the introduction of ETD. These results are well consistent with those from XPS, FTIR, NMR, and other analyses.

Table S2. Comparison of the photocatalytic hydrogen production performance for EHTD-CN and other recently reported carbon nitrides.

Photocatalyst	Strategy	Light source	Catalyst/ cocatalyst	Sacrificial agent	HER (μmol g^{-1} h^{-1})	Enhancement factor	Reference
(Methyl, hydroxyl)-PHI/g-C_3N_4	Post-treatment	300W Xe lamp (≥ 400 nm)	50 mg/1 wt% Pt	10 vol% TEOA	1002	7.2	[13]
Polyelectrolytes/hydroxyl-g-C_3N_4	Self-assembly	300W Xe lamp (≥ 400 nm)	10 mg/1.5 wt% Pt	10 vol% TEOA	24010	14.6	[14]
(C, hydroxyl)-g-C_3N_4	Co-polymerization	300W Xe lamp (≥ 420 nm)	20 mg/1.5 wt% Pt	10 vol% TEOA	7282	17.5	[15]
Thiophene ring-doped g-C_3N_4	Co-polymerization	300W Xe lamp (≥ 420 nm)	50 mg/3 wt% Pt	10 vol% TEOA	10341	15.2	[16]
Aromatic rings-doped g-C_3N_4	Co-polymerization	300W Xe lamp (≥ 420 nm)	50 mg/3 wt% Pt	10 vol% TEOA	2042	3.5	[17]
B-doped D-A integrated g-C_3N_4	Co-polymerization	300W Xe lamp (≥ 420 nm)	30 mg/3 wt% Pt	10 vol% TEOA	1914	5.9	[18]
N-heterobenzene-doped g-C_3N_4	Co-polymerization	300W Xe lamp (≥ 420 nm)	50 mg/1 wt% Pt	10 vol% TEOA	5732	8.4	[19]
Corrugated g-C_3N_4 nanosheet	Post-treatment	300W Xe lamp (≥ 420 nm)	20 mg/0.5 wt% Pt	10 vol% TEOA	2485	40	[20]
P-doped low-crystalline, high-crystalline homojunction	Molten salt method	300W Xe lamp (AM 1.5)	10 mg/MoS_2	20 vol% lactic acid	12090	40.3	[21]
(cyanamide/cyano)- g-C_3N_4	Molten salt method	300W Xe lamp (≥ 420 nm)	20 mg/3 wt% Pt	10 vol% TEOA	3550	13.8	[22]
Ultrathin g-C_3N_4	Supramolecular assembly	300W Xe lamp (≥ 400 nm)	20 mg/3 wt% Pt	10 vol% TEOA	2590	9.9	[23]
Few-layer g-C_3N_4	Supramolecular assembly	300W Xe lamp (≥ 420 nm)	20 mg/1 wt% Pt	20 vol% TEOA	7990	26	[24]
Corrugated g-C_3N_4 nanosheet	Supramolecular assembly	300W Xe lamp (≥ 420 nm)	10 mg/0.5 wt% Pt	10 vol% TEOA	5553	12	[25]
g-C_3N_4 bending nanotube	Supramolecular assembly	300W Xe lamp (≥ 420 nm)	50 mg/1 wt% Pt	10 vol% TEOA	4350	15.8	[26]
Porous V_N-g-C_3N_4	Supramolecular assembly	300W Xe lamp (≥ 400 nm)	20 mg/1 wt% Pt	10 vol% TEOA	5500	17.2	[27]
C-doped hollow porous g-C_3N_4	Supramolecular assembly	300W Xe lamp (≥ 420 nm)	50 mg/1 wt% Pt	10 vol% TEOA	16690	139	[28]
O-doped g-C_3N_4 nanosheet	Supramolecular assembly	300W Xe lamp (≥ 420 nm)	50 mg/3 wt% Pt	10 vol% TEOA	1968	11.3	[29]
P-doped g-C_3N_4 tube	Supramolecular assembly	300W Xe lamp (≥ 420 nm)	100 mg/1 wt% Pt	20 vol% methanol	670	7	[30]

(C, O)-doped g-C_3N_4 nanobelt	Supramolecular assembly	300W Xe lamp (≥ 420 nm)	5 mg/3 wt% Pt	10 vol% TEOA	18380	79.9	[31]
(B-doped, cyano)-g-C_3N_4 tube	Supramolecular assembly	300W Xe lamp (≥ 420 nm)	25 mg/3 wt% Pt	10 vol% TEOA	789	4	[32]
Benzene-ring-doped g-C_3N_4 tube	Supramolecular assembly	300W Xe lamp (≥ 420 nm)	50 mg/1 wt% Pt	10 vol% TEOA	2780	14.9	[33]
(Benzene-ring, O)-doped g-C_3N_4	Supramolecular assembly	300W Xe lamp (AM 1.5)	10 mg/3 wt% Pt	10 vol% TEOA	13920	3.7	[34]
Porous amino-rich g-C_3N_4	Supramolecular assembly	300W Xe lamp (≥ 420 nm)	50 mg/3 wt% Pt	10 vol% TEOA	3270	6	[35]
BTH doped D-A structural g-C_3N_4	Supramolecular assembly	300W Xe lamp (≥ 420 nm)	50 mg/1 wt% Pt	10 vol% TEOA	3950	13.3	[36]
(Hydroxyl, carboxyl)-doped g-C_3N_4	Supramolecular assembly	Xe lamp (≥ 420 nm)	20 mg/2 wt% Pt	30 vol% methanol	985	/	[37]
(Thiophene ring, cyano)-doped g-C_3N_4	Supramolecular assembly	300W Xe lamp (≥ 420 nm)	20 mg/3 wt% Pt	20 vol% TEOA	4177	17.9	[38]
Mesopores homojunction	Supramolecular assembly	300W Xe lamp (≥ 420 nm)	20 mg/3 wt% Pt	10 vol% TEOA	934	5	[39]
Nanotube/nanosheet homojunction	Supramolecular assembly	300W Xe lamp (≥ 420 nm)	10 mg/3 wt% Pt	10 vol% TEOA	9100	22.8	[40]
Nanodot/nanosheet homojunction	Supramolecular assembly	300W Xe lamp (AM 1.5)	10 mg/3 wt% Pt	10 vol% TEOA	21794	10.6	[41]
Pt-N_3/g-C_3N_4	Supramolecular assembly	300W Xe lamp (≥ 420 nm)	20 mg/none	10 vol% TEOA	9750	15.4	[42]
Ag-N_2C_2/g-C_3N_4	Supramolecular assembly	300W Xe lamp (≥ 420 nm)	20 mg/none	10 vol% TEOA	1866	/	[43]
Ag_1Co_1-g-C_3N_4	Supramolecular assembly	300W Xe lamp (≥ 420 nm)	20 mg/none	10 vol% TEOA	1190	/	[44]
C dots/S-doped g-C_3N_4 tube/NiPc	Supramolecular assembly	300W Xe lamp (AM 1.5)	5 mg/1 wt% Pt	10 vol% TEOA	16363	23.2	[45]
Curled g-C_3N_4 nanobelt (NTD-CN)	Supramolecular assembly	300W Xe lamp (≥ 420 nm)	50 mg/3 wt% Pt	10 vol% TEOA	440	4.4	This work
(ETD, HTD)-synergetic g-C_3N_4	Supramolecular assembly	300W Xe lamp (≥ 420 nm)	50 mg/3 wt% Pt	10 vol% TEOA	3090	30.9	This work

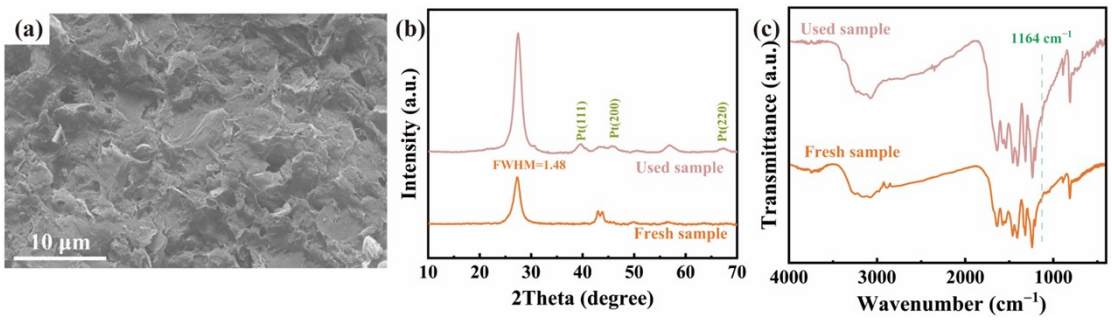

Figure S14. (a) SEM image of used EHTD-CN after recycling tests, (b) XRD patterns and (c) FTIR spectra of fresh sample and used sample.

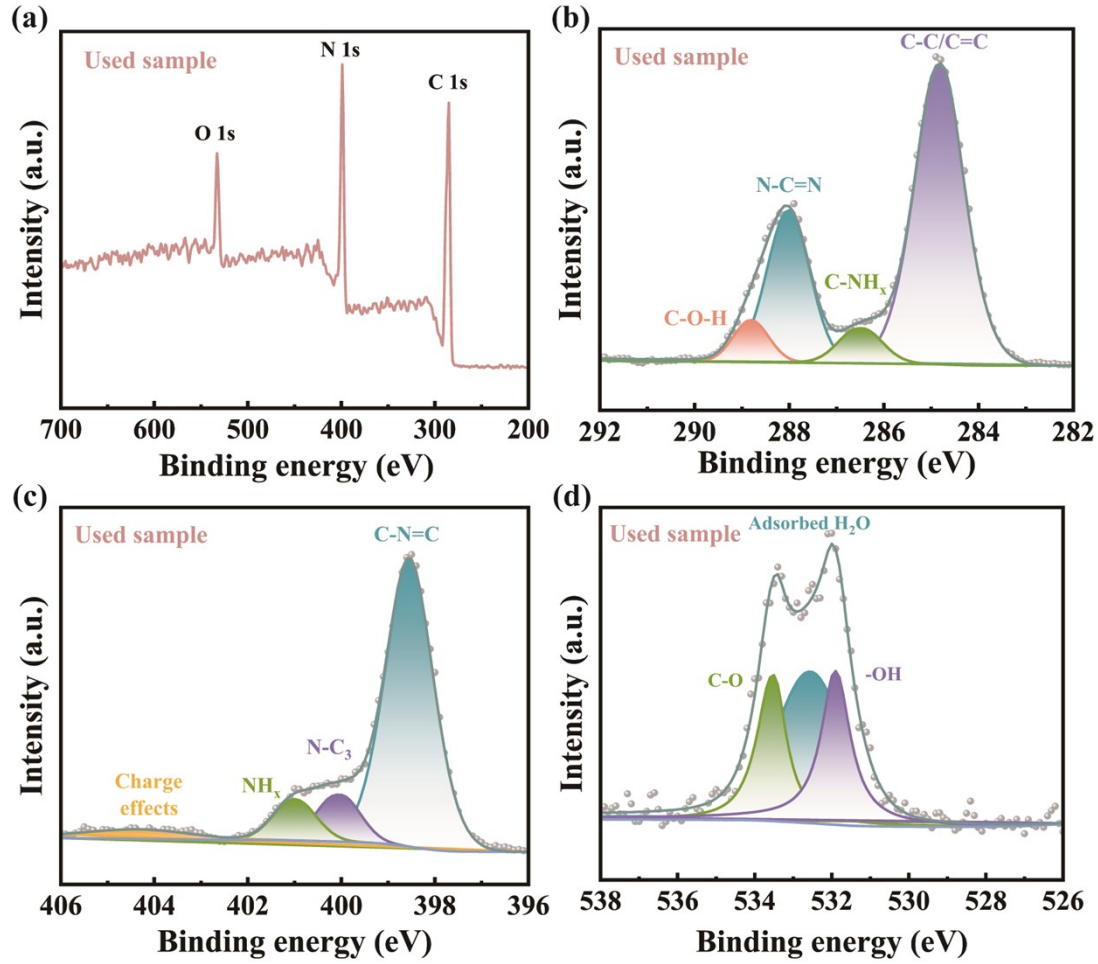

Figure S15. XPS spectra of used sample after 12 h cycling experiments, (a) full survey spectra, (b) C 1s, (c) N 1s, (d) O 1s high-resolution spectra.

As shown in Figure S15, the XPS survey spectrum of post-cycling samples confirms the exclusive presence of C, N, and O elements. High-resolution C 1s deconvolutions exhibit four characteristic peaks at 284.8, 286.47, 288.1, and 288.81 eV, assigned to C-

C/C=C from adventitious carbon or pyrimidine structures, terminal C-NH_x, sp^2 hybridized N-C=N, and C-OH, respectively. High-resolution N 1s spectrum exhibits characteristic peaks corresponding to C-N=C, N-C_3, NH_x, and π excitation, respectively. High-resolution O 1s spectrum resolve three components at 531.89, 532.56, and 533.50 eV, assigned to hydroxyl groups (-OH), surface-adsorbed H_2O, and C-O, respectively. The robust BIEF with EHTD-CN facilitates monodisperse distribution of Pt cocatalysts and its low loading amount, resulting in no discernible Pt signals in XPS spectrum. These results demonstrate unchanged chemical composition after 12 h operation, underscoring its exceptional structural integrity and high practical applicability. Notably, relative to the pristine g-C_3N_4, positive binding energy shifts in heptazine rings and terminal NH_x groups attributes to h^+ accumulation at HTD sites (oxidation centers). Concurrently, slight positive shifts of binding energy in C-O/-OH results from electron extraction from ETD (photogenerated electron-rich sites) by Pt nanodots with high work function.

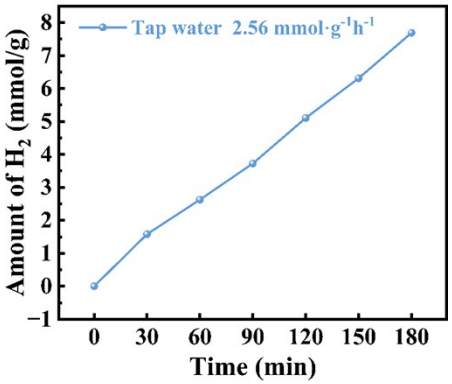

374

375 **Figure S16.** Photocatalytic hydrogen evolution curve of EHTD-CN in tap water.

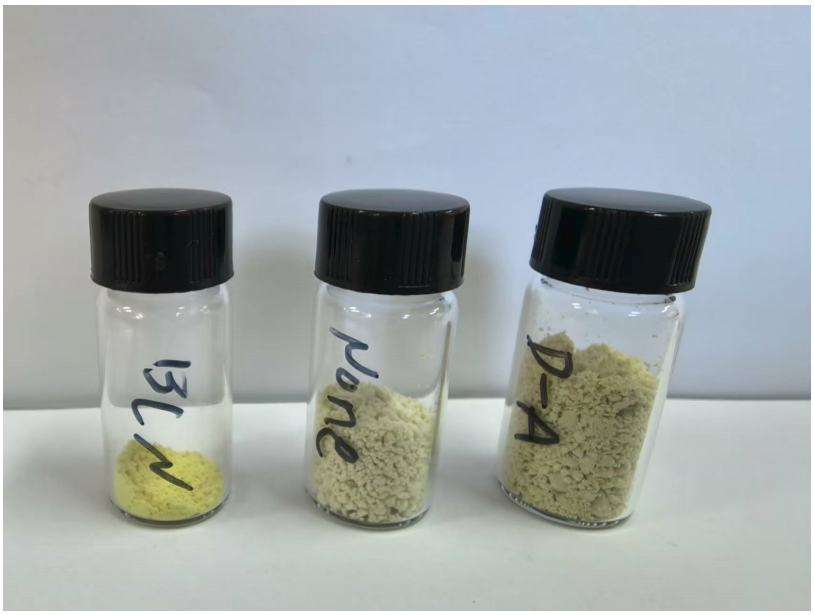

376

377 **Figure S17.** Macroscopic photograph of 0.1g of BCN (left), NTD-CN (middle), and EHTD-CN (right).

378

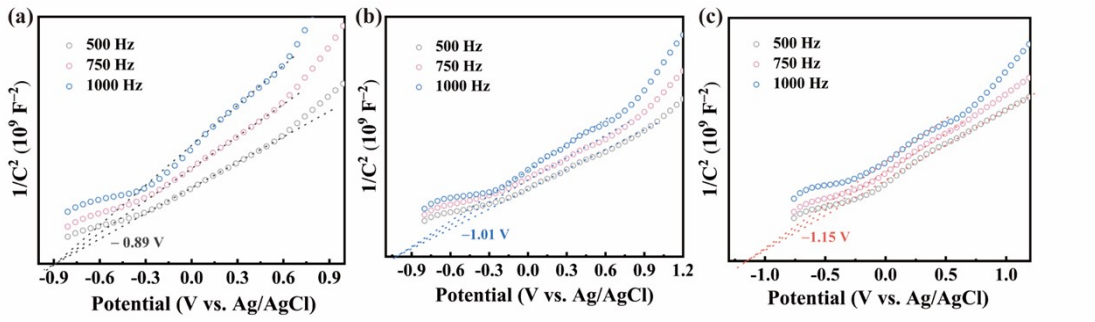

379

380 **Figure S18.** Mott-Schottky curves of (a) BCN, (b) NTD-CN and (c) EHTD-CN.

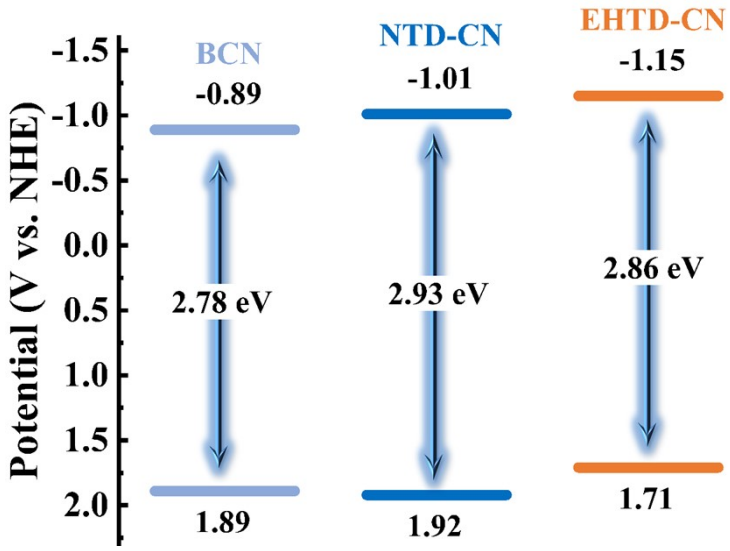

381

382 **Figure S19.** Schematic band structure of BCN, NTD-CN and EHTD-CN.

383 As evidenced by the Mott-Schottky plots in Figure S17, all samples exhibit positive
384 slopes across three measured frequencies, confirming n-type semiconductor
385 behavior. In addition, the flat-band potential of BCN, NTD-CN, and EHTD-CN,
386 evaluated from the tangent intercept of linear portions with the x-axis, are measured
387 as –0.89, –1.01, and –1.15 V vs. Ag/AgCl, respectively. Converting these values to the
388 normal hydrogen electrode (NHE) via Equation S9 gives –0.89, –1.01, and –1.15 V vs.
389 NHE. For n-type semiconductors, the conduction band minimum (CBM) is typically 0.2
390 eV more negative than its flat-band potential. Thus, their CBM are estimated to be
391 –0.89, –1.01, and –1.15 V vs. NHE, respectively. Subsequently, their valence band
392 maxima are calculated as 1.89, 1.92, and 1.71 V vs. NHE, respectively.

The resulting band alignments are schematically illustrated in Figure S18. Quantum confinement in ultrathin curled nanobelts widens the bandgap of NTC-CN. EHTD-CN displays a more negative CBM, thermodynamically favoring proton reduction to H_2.

$$E_{NHE} = E_{Ag/AgCl} + 0.197\ V \quad \text{(Equation S13)}$$

$$E_{VB} - E_{CB} = E_g \quad \text{(Equation S14)}$$

Moreover, according to the equation S11:

$$E_{VB\text{-}NHE} = \Psi + E_{VB\text{-}XPS} - 4.44 \quad \text{(Equation S15)}$$

where Ψ is the instrumental work function (4.5 eV). The obtained $E_{VB\text{-}XPS}$ potential can be converted into $E_{VB\text{-}NHE}$, thus the VBM potentials of BCN, NTD-CN and EHTD-CN are 1.85 V, 1.90 V, and 1.70 V vs. NHE, respectively. These results are almost consistent with the band structure obtained from Mott-Schottky curves, further confirming their reliability.

Table S3. Slope values obtained from the Mott-Schottky plots at 1000 Hz for BCN, NTD-CN, and EHTD-CN.

Samples	Slope values
BCN	2.21×10^{11}
NTD-CN	9.43×10^{10}
EHTD-CN	4.75×10^{10}

Furthermore, charge carrier densities were quantified via the slope of Mott-Schottky curves at 1000 Hz (Text S1.8). Generally, a smaller slope unequivocally reflects a higher charge carrier density. Owing to the robust BIEF, EHTD-CN exhibits the smallest Mott-Schottky slope, thereby evidencing its largest charge carrier density.

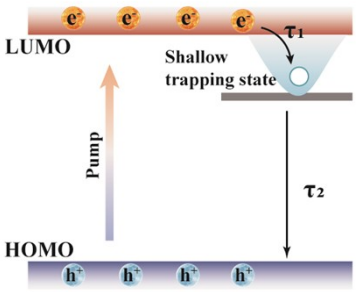

412

413 **Figure S20.** Schematic diagram of TA signal at different timescales for BCN.

414

415 **Table S4.** The fitted decay dynamics of BCN and EHTD-CN.

Component	τ_1 (ps)	A_1 (%)	τ_2 (ps)	A_2 (%)	τ_3 (ps)	A_3 (%)	τ_{ave} (ps)
BCN	146.44	11.94	1296.49	88.06	/	/	1159
EHTD-CN	106.64	2.45	535.88	11.45	3144.35	86.10	2771

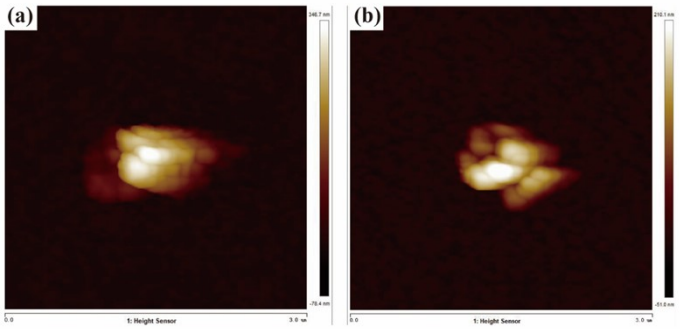

Figure S21. KPFM surface morphologies of BCN and EHTD-CN.

To accurately probe exciton dissociation and charge carrier dynamics, KPFM measurements were conducted on the regions with comparable microstructure and height profiles, eliminating the potential artifacts from topographic variations or sample content. Figure 6a–d reveal positive surface potential signals across all samples due to electron transfer to the ITO substrate, a characteristic manifestation of n-type semiconductor behavior (potential scale uniformly calibrated). The synergy of ETD and HTD enhances polarization within EHTD-CN, yielding a stronger contact potential difference (–76.6 mV), which manifests as a pronounced low-potential regions at the center of its potential distribution mapping. Upon illumination, the robust BIEF in EHTD-CN promotes efficient exciton dissociation into free charge carriers, consequently indicating a more significant decrease in contact potential difference compared to BCN.

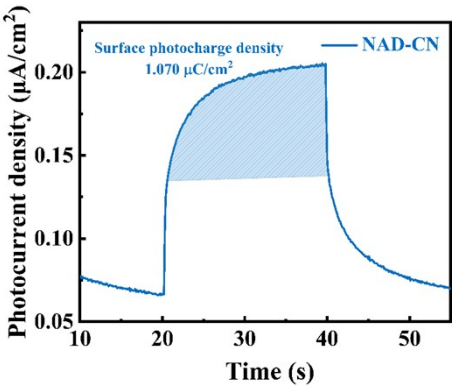

431

432 **Figure S22.** Surface photocharge density of NTD-CN.

433

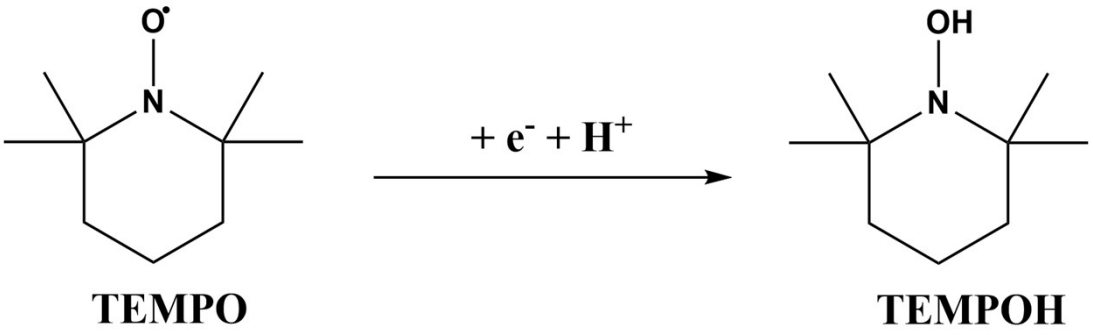

434

435 **Figure S23.** Schematic diagram of the conversion process for the reduction of TEMPO to TEMPOH
436 by electrons.

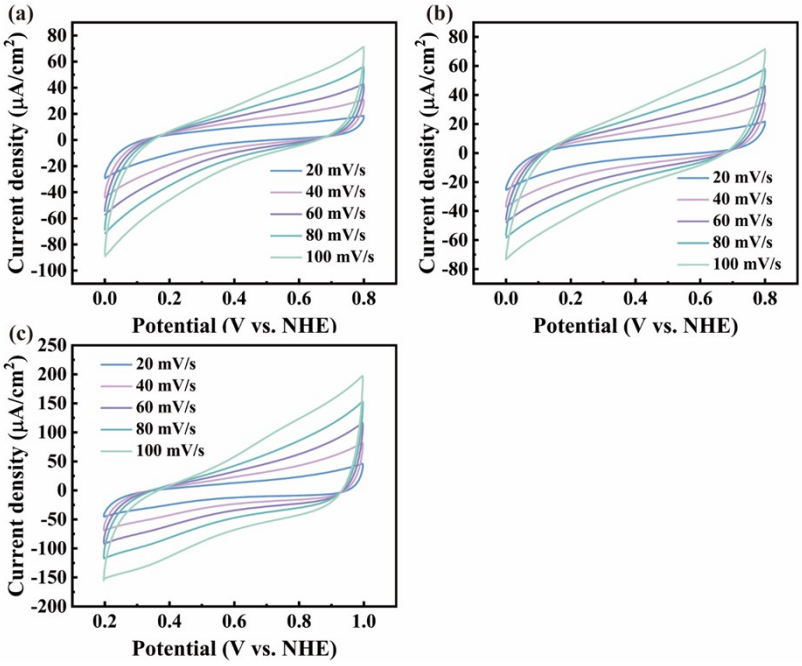

Figure S24. Cyclic voltammetry curves of (a) BCN, (b) NTD-CN and (c) EHTD-CN at different scan rates.

Cyclic voltammetry (CV) measurements for BCN, NTD-CN, and EHTD-CN were performed. Generally, a larger integrated area in CV curves reflects a higher specific capacitance, signifying greater number of electrons available for reduction [46]. Variations in scan rate do not alter the characteristic shape of CV curves. However, as the scan rates increase, the current density and corresponding CV curve area increase for all samples. Notably, EHTD-CN exhibits a substantially larger CV curve area compared to BCN and NTD-CN, indicating a greater population of available free electrons. The double-layer capacitances (C_{dl}), proportional to the electrochemically active surface area (ECSA), were determined by fitting the linear relationship between the scan rate and current density. NTD-CN shows only a marginal enhancement in ESCA relative to BCN. In stark contrast, EHTD-CN demonstrates a significantly increased ECSA. This trend in ESCA directly correlates with the photocatalytic hydrogen production, highlighting that the simultaneous incorporation of ETD and HTD markedly increases the density of active sites on the photocatalyst surface.

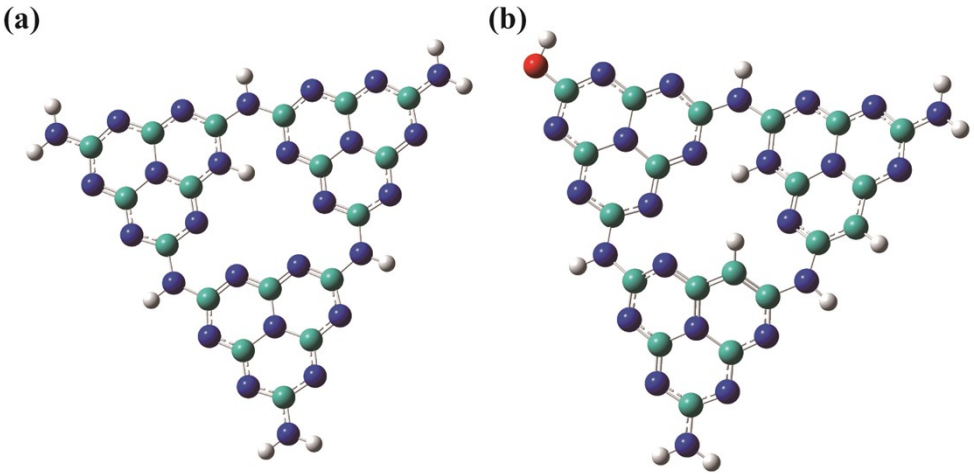

454

455 **Fig. S25.** The calculation model of H* adsorption free energy for (a) BCN and (b) EHTD-CN. (N, blue; C,
456 cyan; O, red; H, white)

Reference

[1] J.H. Zhao, R.H. Mu, Y. Zhang, Z.D. Yang, H.X. Zhang, H. Shi, M. Zhang, Z.F. Zheng, P.J. Yang, J Mater Chem A 10 (2022) 16873–16882.

[2] D.D. Zheng, J.M. Zhou, Z.P. Fang, T. Heil, A. Savateev, Y.F. Zhang, M. Antonietti, G.G. Zhang, X.C. Wang, J Mater Chem A 9 (2021) 27370–27379.

[3] H.T. Wang, J.Z. Jiang, L.L. Yu, J.H. Peng, Z. Song, Z.G. Xiong, N. Li, K. Xiang, J. Zou, J.P. Hsu, T.Y. Zhai, Small 19 (2023) 2301116.

[4] Q.X. Zhou, Y. Guo, Z.Q. Ye, Y.Z. Fu, Y. Guo, Y.F. Zhu, Mater. Today 58 (2022) 100–109.

[5] G.Q. Zhang, Y.S. Xu, G.S. Liu, Y.L. Li, C.X. He, X.Z. Ren, P.X. Zhang, H.W. Mi, Chinese Chem. Lett. 34 (2023) 107383.

[6] C.X. Shi, R.L. Pan, J.L. Yuan, C.B. Liu, Adv. Funct. Mater. 35 (2025) 2500342.

[7] Y. Guo, S.J. Huang, Y. Guo, Z.Q. Ye, J. Nan, Q.X. Zhou, Y.F. Zhu, Appl. Catal. B-Environ. 312 (2022) 121388.

[8] L.H. Xia, Z.L. Sun, Y.N. Wu, X.F. Yu, J.B. Cheng, K.S. Zhang, S. Sarina, H.Y. Zhu, H. Weerathunga, L.X. Zhang, J.F. Xia, J.Q. Yu, X.L. Yang, Chem. Eng. J. 439 (2022) 135668.

[9] H. Yang, S.D. Sun, J.L. Lyu, Q. Yang, J. Cui, Chem. Eng. J. 481 (2024) 148297.

[10] S.H. Meng, J.L. Li, S.Y. Wang, S.H. Zhan, W.P. Hu, Y. Li, Adv. Mater. 37 (2025) 2500342.

[11] H. Yang, S.D. Sun, Q. Yang, J. Cui, Nano Mater. Sci. 8 (2026) 364–437.

[12] Q. Liu, H. Cheng, T.X. Chen, T.W. Benedict Lo, Z.M. Xiang, F.X. Wang, Energy & Environmental Science 15 (2022) 225–233.

[13] L.H. Mao, B.J. Zhai, J.W. Shi, X. Kang, B.R. Lu, Y.B. Liu, C. Cheng, H. Jin, E. Lichtfouse, L.J. Guo, ACS Nano 18 (2024) 13939–13949.

[14] L. Yang, W. Zhou, M.S. Dou, X. Yue, Y.Z. Hu, T.P. Lu, Y. He, Y.Y. Du, A.N. Zhu, H.K. Yang, S.L. Lu, X.D. Chen, Adv. Funct. Mater. 35 (2025) 2500415.

[15] Z.M. Zhai, H.H. Zhang, F.S. Niu, P.Y. Liu, J.J. Zhang, H.B. Lu, ACS Nano 16 (2022) 21002–21012.

[16] S. Zhao, D.Y. An, Y.M. Zhou, J.S. Fang, S.P. Zhuo, Appl. Catal. B-Environ. Energy 358 (2024) 124397.

[17] K. Li, M. Sun, W.D. Zhang, Carbon 134 (2018) 134–144.

[18] T.Y. Zhou, T.T. Li, J.Y. Hou, Y.B. Wang, B. Hu, D.S. Sun, Y.Y. Wu, W. Jiang, G.B. Che, C.B. Liu, Chem. Eng. J. 445 (2022) 136643.

[19] Z.X. Ma, X.P. Zong, Q. Hong, L.J. Niu, T.Y. Yang, W.S. Jiang, D. Qu, L. An, X.Y. Wang, Z.H. Kang, Z.C. Sun, Appl. Catal. B-Environ. 319 (2022) 121922.

[20] D.C. Jiang, S.N. Hu, Y. Qu, X. Tian, H.W. Du, C.H. Zhu, Z.J. Li, L.S. Yin, Y.P. Yuan, G. Liu, Adv. Funct. Mater. 34 (2024) 2311803.

[21] X.H. Wang, S. Xue, T.Y. Shi, Z.M. Zhao, A.L. Song, G.C. Li, L. Wang, J.F. Huang, A.L. Meng, Z.J. Li, Adv. Funct. Mater. 35 (2025) 2424853.

[22] Z.H. Yu, X.Y. Yue, J.J. Fan, Q.J. Xiang, ACS Catal. 12 (2022) 6345–6358.

[23] L.Y. Wang, Y.Z. Hong, E.L. Liu, X.X. Duan, X. Lin, J.Y. Shi, Carbon 163 (2020) 234–243.

[24] Y.T. Xiao, G.H. Tian, W. Li, Y. Xie, B.J. Jiang, C.G. Tian, D.Y. Zhao, H.G. Fu, Journal of the American Chemical Society 141 (2019) 2508–2515.

[25] G.G. Zhao, B.W. Li, X.N. Yang, X.M. Zhang, Z.F. Li, D.C. Jiang, H.W. Du, C.H. Zhu, H.Q. Li, C. Xue, Y.P. Yuan, Adv. Powder Mater. 2 (2023) 100077.

[26] Y.F. Wan, J. Zhang, J.W. Chen, Z.J. Liu, J.L. Fan, J. Zhang, G. Wang, R.L. Wang, Chem. Eng. J. 417 (2021) 127956.
[27] Q.C. Li, Y.W. Tong, Y.B. Zeng, X.K. Gu, M.Y. Ding, Chem. Eng. J. 450 (2022) 138010.
[28] D. Liu, C.L. Li, C.Y. Zhao, Q. Zhao, T.Q. Niu, L.K. Pan, P.W. Xu, F.Q. Zhang, W.D. Wu, T.J. Ni, Chem. Eng. J. 438 (2022) 135623.
[29] J.W. Zhang, S. Gong, N. Mahmood, L. Pan, X.W. Zhang, J.J. Zou, Appl. Catal. B-Environ. 221 (2018) 9–16.
[30] S.E. Guo, Z.P. Deng, M.X. Li, B.J. Jiang, C.G. Tian, Q.J. Pan, H.G. Fu, Angew. Chem. Int. Ed. 55 (2016) 1830–1834.
[31] J.J. Wu, N. Li, X.H. Zhang, H.B. Fang, Y.Z. Zheng, X. Tao, Appl. Catal. B-Environ. 226 (2018) 61–70.
[32] L. Chen, Y.X. Wang, S. Cheng, X.L. Zhao, J.Q. Zhang, Z.M. Ao, C.C. Zhao, B. Li, S.J. Wang, S.B. Wang, H.Q. Sun, Appl. Catal. B-Environ. 303 (2022) 120932.
[33] S.S. Li, Y.N. Peng, C. Hu, Z.H. Chen, Appl. Catal. B-Environ. 279 (2020) 119401.
[34] G.Y. Wu, Z.Y. He, Q.H. Wang, H.B. Wang, Z.Y. Wang, P.P. Sun, Z. Mo, H.Z. Liu, H. Xu, Journal of Materials Science & Technology 195 (2024) 1–8.
[35] T. Huang, J.Q. Chen, L.L. Zhang, A. Khataee, Q.F. Han, X.H. Liu, J.W. Sun, J.W. Zhu, S.G. Pan, X. Wang, Y.S. Fu, Chinese Journal of Catalysis 43 (2022) 497–506.
[36] Z.J. Liu, J. Zhang, Y.F. Wan, J.W. Chen, Y.F. Zhou, J. Zhang, G. Wang, R.L. Wang, Chem. Eng. J. 430 (2022) 132725.
[37] G.M. Gao, L.N. Zhang, Q.F. Chen, H.L. Fan, J. Zheng, Y.F. Fang, R. Duan, X.F. Cao, X. Hu, Chem. Eng. J. 409 (2021) 127370.
[38] R.L. Liu, J.Y. Lin, L.L. Zhu, X.X. Zhang, Y. Li, H. Pan, L.T. Kong, S.M. Zhu, J. Wang, Chem. Eng. J. 484 (2024) 149507.
[39] G.M. Ba, Z.W. Liang, H.P. Li, N. Du, J.Q. Liu, W.G. Hou, Appl. Catal. B-Environ. 253 (2019) 359–368.
[40] G.Y. Wu, W. Zhang, Z. Mo, X.Y. Zhao, P.P. Sun, Q.H. Wang, P.C. Yan, X.J. She, H. Xu, ACS Catal. 15 (2025) 8822–8832.
[41] X.L. Zhu, E.L. Zhou, X.S. Tai, H.B. Zong, J.J. Yi, Z.M. Yuan, X.L. Zhao, P. Huang, H. Xu, Z.Y. Jiang, Angew. Chem. Int. Edit. 64 (2025) 202425439.
[42] D.J. Liu, C.Y. Zhang, J.W. Shi, X.D. Jin, W. Liu, M.C. Liu, Y.B. Chen, L.J. Guo, Appl. Catal. B-Environ. Energy 361 (2025) 124655.
[43] X.H. Jiang, L.S. Zhang, H.Y. Liu, D.S. Wu, F.Y. Wu, L. Tian, L.L. Liu, J.P. Zou, S.L. Luo, B.B. Chen, Angew. Chem. Int. Ed. 59 (2020) 23112–23116.
[44] Y.Z. Liu, Y. Sun, E. Zhao, W.W. Yang, J.K. Lin, Q. Zhong, H.F. Qi, A.X. Deng, S.G. Yang, H.Y. Zhang, H. He, S.M. Liu, Z.P. Chen, S.B. Wang, Adv. Funct. Mater. 33 (2023) 2301840.
[45] X. Miao, P. Zhang, B.L. Wang, X. Bai, W.S. Liu, Appl. Catal. B-Environ. Energy 357 (2024) 124268.
[46] Y.F. Shao, X.Q. Hao, S.D. Lu, Z.L. Jin, Chem. Eng. J. 454 (2023) 140123.